HiSST: 3rd International Conference on
High-Speed Vehicle Science & Technology

14–19 April 2024, Busan, Korea

Direct Numerical Simulation of Supersonic Reacting Mixing Layers

Nicholas N. Gibbons[1], *Lachlan Whyborn*,[1] *Vincent Wheatley*[1]

Abstract

A pair of high fidelity direct numerical simulations have been developed to study the interaction between turbulence and chemistry in high-speed combustion. One case considers a time-developing hydrogen/air turbulent mixing layer taken from the literature, aiming to verify and demonstrate a newly improved high-fidelity numerical scheme, and the other will investigate a hydrocarbon, i.e. ethylene, combustion at effectively the same conditions. The numerical method that has been developed uses a novel technique for detecting discontinuities to hybridise a low dissipation, central inviscid flux scheme, with a high-dissipation, shock capturing scheme. The method is successfully verified against the analytic solution for a steepening nonlinear wave, then applied to the two mixing layer cases. The results show a number of striking differences between the hydrogen and ethylene cases, including very different regimes of premixed vs. nonpremixed combustion and different patterns of heat release over time. Conditional statistics also show both cases have large variations in temperature that are not correlated with mixture fraction, an important finding that will need to be addressed in model developments for highly compressible combustion flows.

Keywords: *Direct Numerical Simulation, Hypersonics, Combustion*

1. Introduction

Simulating the supersonic combustion in a scramjet is a problem that combines compressible fluid dynamics, turbulence, and combustion into a difficult numerical modelling challenge. A key element of this challenge is the interaction between the chaotic motion of turbulence and the nonlinear mixing and chemical reactions that occur in combustion, particularly since the true details of the turbulence are generally not available in a full scale calculation. Without a detailed description of the turbulence, scramjet calculations rely on approximate models for their turbulence chemistry interaction, often ones that are adapted from low-speed calculations, which are not always suitable for highly compressible flow. This problem was studied by Ref. [1], who surveyed a number of supersonic combustion models and also analysed a the combustion regimes present in scramjet-like flow paths, concluding that supersonic turbulence chemistry models will have to span a wide range of regimes and handle complex mixing phenomena that are neither truly premixed or non-premixed.

Further interest in this topic has been spurred by developments in compressible combustion modelling. Additionally, much of the literature surveyed in Ref. [1] considers hydrogen fuel, which has high energy per kilogram but poor energy per cubic meter, making it unsuitable for cruise vehicles where tight packaging of the airframe is critical. For these reasons, the work in this paper proposes to extend the work of Ref. [1] by first replicating their mixing-layer simulations in hydrogen, and then comparing these results to a similar flow that uses a simple hydrocarbon fuel, in this case ethylene. These mixing layers are treated with highly resolved direct numerical simulations (DNS) that account for all of the physics of turbulent combustion, which enables us to analyse the resulting combustion physics in great detail. Comparing the hydrogen and hydrocarbon simulations will also give insight into the relationship between the two types of combustion specifically, and also the physics of compressible hydrocarbon flames in general.

[1] *School of Mechanical and Mining Engineering, University of Queensland, St. Lucia QLD 4072, Australia*

2. Numerical Method

Simulations in this paper are performed using Eilmer [2], an open-source compressible flow simulation code developed at the University of Queensland. Eilmer is specialised for research applications in high-speed and hypersonic flow, and has recently been equipped with low-dissipation numerics that are suitable for Large Eddy and Direct Numerical Simulation (LES/DNS) [3]. Eilmer solves the compressible Navier-Stokes equations for a 3D viscous fluid in the continuum limit, and also a set of species transport equations, one for each chemical species in the reaction mechanism.

$$\frac{\partial \rho}{\partial t} + \frac{\partial}{\partial x_j}(\rho u_j) = 0 \tag{1}$$

$$\frac{\partial}{\partial t}(\rho u_i) + \frac{\partial}{\partial x_j}(\rho u_j u_i) = -\frac{\partial p}{\partial x_i} + \frac{\partial \tau_{ji}}{\partial x_j} \tag{2}$$

$$\frac{\partial}{\partial t}\left(E\right) + \frac{\partial}{\partial x_j}\left[(E+p)u_j\right] = \frac{\partial}{\partial x_j}(u_i t_{ij}) - \frac{\partial q_j}{\partial x_j} \tag{3}$$

$$\frac{\partial \rho_s}{\partial t} + \frac{\partial}{\partial x_j}(\rho_s u_j) + \frac{\partial}{\partial x_j}(v_{sj}) = \dot{\omega}_s \tag{4}$$

These equations are solved by discretising the set partial differential equations onto a mesh or grid of finite-volume elements, resulting in an integral form where the change in a vector of conserved variables **U** is affected by the combination of convective and viscous fluxes ($\mathbf{F}^c$ and $\mathbf{F}^v$) flowing through each interface, and also the integral of the source terms **Q** throughout the cell's volume.

$$\frac{\partial}{\partial t}\int_V \mathbf{U}\, dV = -\oint_S (\mathbf{F}^c - \mathbf{F}^v)\cdot \hat{n}\, dA + \int_V \mathbf{Q}\, dV \tag{5}$$

For the unsteady, high-frequency flow encountered in a Direct Numerical Simulation, these equations are solved explicitly, using a three-stage Runge Kutta scheme that is third-order accurate in time. The effect of the chemical source terms is treated separately using so-called operator splitting, in which a separate adaptive explicit integrator is used to substep the chemistry independently between each fluid time step [4].

For the details of solving these transport equations the reader is referred to Ref. [2], though in this paper the convective flux term $\mathbf{F}^c$ deserves some special attention, as it has been modified to accommodate the low-dissipation scheme needed for high-quality DNS. The key detail is the implementation of the Summation-by-Parts Alpha-Split Flux (ASF) scheme, originally developed for finite difference codes by Ref. [5] and adapted for finite-volume work by Ref. [6]. This scheme isdeveloped by first recognising that a typical convective flux is a derivative of a pair of quantities multiplied together, typically a scalar and a velocity component.

$$\mathbf{F}^c = \frac{\partial \rho u}{\partial x} \tag{6}$$

This expression can be factored using the familiar product rule of vector calculus, to generate a sum of single variable derivatives that is mathematically equivalent to the original form. The core insight of the ASF method is that these two representations of the same quantity are not *numerically* identical, and can be discretised differently and then combined, using a splitting parameter α. This quantity gives the method its name.

$$\mathbf{F}^c = \alpha\frac{\partial \rho u}{\partial x} + (1-\alpha)\left[\rho\frac{\partial u}{\partial x} + u\frac{\partial \rho}{\partial x}\right] = \alpha\mathbf{F}^c_{div} + (1-\alpha)\mathbf{F}^c_{prod} \tag{7}$$

The first component is the so-called *divergence* term $\mathbf{F}^c_{div}$, which is discretised using a finite difference at the relevant face and multiplied by α. The second component is the so-called *product rule* term $\mathbf{F}^c_{prod}$, which is discretised as a source term that is integrated over the cell. The stencil coefficients for a finite-volume grid have been derived in [6], and are as follows, assuming the flux is computed at an interface located between cells i and $i+1$.

$$\begin{aligned}\mathbf{F}^c_{div} &= \frac{1}{12}\left[-\rho_{i-1}u_{i-1} + 7\rho_i u_i + 7\rho_{i+1}u_{i+1} - \rho_{i+2}u_{i+2}\right] \\ \mathbf{F}^c_{prod} &= \frac{1}{12}\left[-\rho_{i-1}u_{i+1} - \rho_{i+1}u_{i-1} + 8\rho_i u_{i+1} + 8\rho_{i+1}u_i - \rho_i u_{i+2} - \rho_{i+2}u_i\right]\end{aligned} \tag{8}$$

With suitable choices of α, the ASF method has been shown give low numerical dissipation and high-order of accuracy, similar to a centred symmetric difference scheme but with better stability at high Reynolds numbers. A slight complicating factor is that each term in the convective flux vector can get its own value of α, with different configurations producing flux schemes with different properties. The simulations in this paper use the entropy conserving scheme of Ref. [7].

The ASF method is a high-order central scheme and so suffers from oscillations near discontinuities such as shock waves. In compressible LES/DNS, it is common to address this issue by detecting the presence of shockwaves and locally blending the high-order flux with a more robust shock-capturing flux calculator, such as the Riemann-solver based AUSMDV method [8], used in this work. Less commonly appreciated is that this is also true at contact discontinuities, a different type of discontinuity that is routinely present in mixing and combustion flows.

To this end, the simulations in this work actually use two novel discontinuity detectors, one for shock waves and one for thermal/density discontinuities, which are used to compute a continuous blending factor between zero and one, S. The flux at a given interface is then computed using:

$$\mathbf{F}^c = S\,\mathbf{F}^c_{AUSMDV} + (1-S)\,\mathbf{F}^c_{ASF} \tag{9}$$

Shockwaves are detected using a method based on the HLLC flux calculator, specifically the ”Hybrid Estimates” wave speeds discussed in [9].

$$q_{L/R} = \begin{cases} 1 & p^*/p_{L/R} \leq 1 \\ \sqrt{1 + \frac{\gamma+1}{2\gamma}\left(\frac{p^*}{p_{L/R}} - 1\right)} & \text{otherwise} \end{cases} \tag{10}$$

$$S_{shock} = min\left(\frac{q-1}{\mathcal{M}}, 1.0\right) \quad : \quad q = max(q_R, q_L) \tag{11}$$

Contact surfaces are detected using a different switch that looks for nonisentropic behaviour in the temperature or density in a stencil of four cells, two on either side of each face. It begins by fitting a linear function to the pressure across the entire stencil, then uses this pressure gradient to isentropically extrapolate the temperatures/densities left to right, then right to left.

$$p_R/p_L = \frac{p_0 + p_1 + p_2 + p_3}{4} \pm \frac{3}{2}\frac{-3p_0 - p_1 + p_2 + 3p_3}{10} \tag{12}$$

$$T_R = T_0\left(\frac{p_R}{p_0}\right)^{(\gamma-1)/\gamma} \quad T_L = T_3\left(\frac{p_L}{p_3}\right)^{(\gamma-1)/\gamma} \tag{13}$$

$$\rho_R = \rho_0\left(\frac{p_R}{p_0}\right)^{1/\gamma} \quad \rho_L = rho_3\left(\frac{p_L}{p_3}\right)^{1/\gamma} \tag{14}$$

The difference between these extrapolated quantities and their actual values is a measure of how much nonisentropic change is happening across the stencil, and so it can be used as the argument to a hyperbolic tangent function that outputs the contact surface detector value $S_{contact}$.

$$\Delta\rho = \frac{|\rho_L - \rho_0|}{\rho_0} + \frac{|\rho_R - \rho_3|}{\rho_3} \tag{15}$$

$$S^{\rho}_{contact} = \frac{1}{2}\tanh\left(6\Delta\rho - 2\right) + \frac{1}{2} \tag{16}$$

And similarly for the temperatures. The final value of the shock detector is then the maximum of all three sensors.

$$S = max(S_{shock}, S^{\rho}_{contact}, S^{T}_{contact}) \tag{17}$$

3. Verification of Numerical Method

In this section we seek to verify that the numerical method for computing the inviscid flux is implemented correctly, and is additionally achieving its goal of delivering small amounts of numerical dissipation. For this purpose we introduce the so-called "Steepening Wave Problem", a canonical compressible flow with an exact analytic solution developed by Ref. [10]. Also called a "Simple Wave", the flow a periodic, one-dimensional wave that begins with the velocity field configured into a sine wave $u_0(x)$, which steepens in time and eventually forms a shock at time t_{shock}. At any time up to this point, the velocity field $u(x)$ can be described by the expression:

$$u(x) = u_0(x)\ sin\left(\pi(x - t(c_0 + \frac{1}{2}(\gamma+1)u(x)))\right) \tag{18}$$

Where c_0 is the reference speed of sound $\sqrt{\gamma R T_0}$. To actually compte the solution at a given time, a nonlinear numerical equation solver can be called at each point x to solve for the appropriate velocity $u(x)$ by ensuring equation 18 is satisfied. With u solved for, the pressure, density, and temperature are then computed using the isentropic flow equations.

$$p(x) = p_0\left(\frac{1+(\gamma-1)u(x)}{2c_0}\right)^{\frac{2\gamma}{\gamma-1}} \quad \rho(x) = \rho_0\left(\frac{1+(\gamma-1)u(x)}{2c_0}\right)^{\frac{2}{\gamma-1}} \quad T(x) = \frac{p(x)}{R\rho(x)} \tag{19}$$

Where the reference quantities used here are $p_0 = 100$ kPa, $rho_0 = 1.0$ kg/m^3, and an ideal gas with $\gamma = 1.4$. Beginning with an initial condition of $u(x)_0 = -c_0 sin(\pi x)$, the flow field has been simulated in Eilmer using both the pure ASF scheme and the shock capturing AUSMDV up to half of the shock formation time t_{shock}, the time at which the wave steepens into a normal shock, given by:

$$t_{shock} = \left|\frac{2}{c_0\pi(\gamma+1)}\right| \tag{20}$$

The simulations were advanced in time using a three stage explicit Runge-Kutta explicit scheme with a nondimensional timestep (CFL) of 0.1, which is sufficient to ensure that the temporal discretisation error is negligible. Additionally, the reconstruction limiters that are needed for simulating flows with discontinuities were disabled, as they pollute the order of accuracy near local maxima and are unnecessary in a smooth flow. Figure 1 shows a snapshot of the ASF simulated flow field against the exact solution, for a discretisation of 32 cells in total.

The error between the numerical and analytic solution is a surprisingly sensitive test for misbehaviour of the inviscid flux scheme. In this work we will consider both the worst case $L_0 = max(|u_n - u_a|)$ error, and the root sum squared $L_2 = \sqrt{(\sum(u_n - u_a)^2/n)}$ error. Of interest is not so much the magnitude of these metrics but their behaviour as the simulation grid is refined: The dissipative AUSMDV scheme

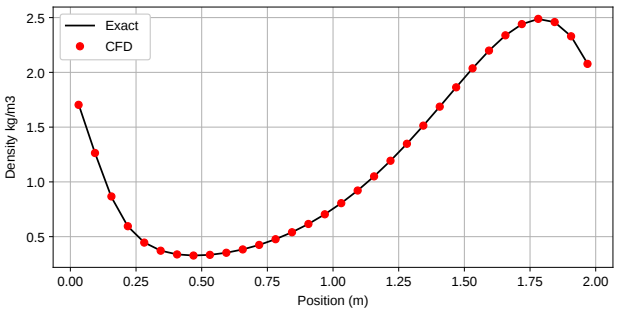

Fig 1. Density flowfield at t = ½ ASF numerical result vs. solution of equation 19.

should be second order, its error reducing nonlinearly as $O(dx^2)$, while the pure ASF scheme should reduce by a factor of $O(dx^4)$. Minor bugs or other implementation errors can easily ruin these theoretical convergence rates, which why is order analysis is a helpful tool in verifying that ones code is free from such mistakes. Figure 2 shows that both schemes in Eilmer display the expected behaviour, using simulations with 32, 64, and 128 cells. Further refinement did not reduce the error in the ASF cases, likely due to the fourth order convergence lowering the error so far that some other, non grid related, error terms comes into play.

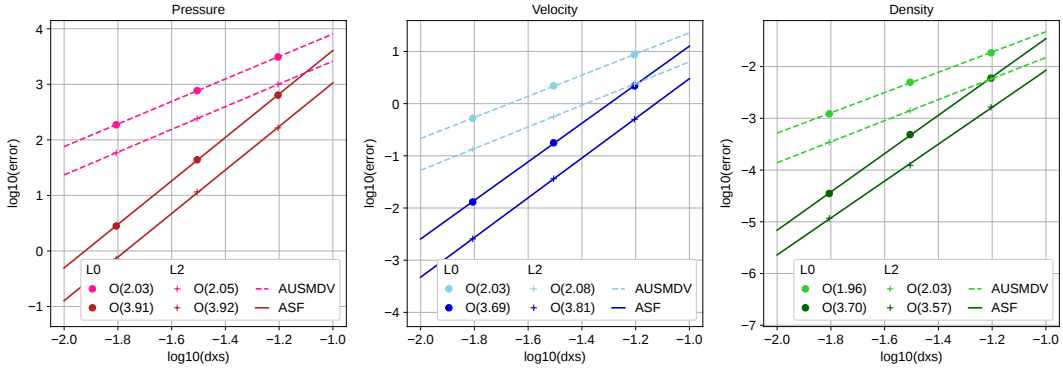

Fig 2. Linear least-squares fit to log-space error: AUSMDV vs. ASF results.

Further analysis is possible using a property of the steepening wave initial condition: namely that it is periodic, which permits a Fourier decomposition into a discrete sum of sine waves. This operation has been performed on both the analytic solution and the two CFD solutions. Figure 3 shows the absolute value of the magnitude in wave space for these three results, which are computed form the n=128 case. As expected the ASF scheme follows the analytic solution well, losing some energy at higher wavenumbers and dissolving into noise at a wave number of about 26. In contrast, the AUSMDV results depart from the solution at a wave number of about 13, and actually shows higher energy content in the resulting noise region. This wavenumber of 13 1/m corresponds to approximately 5 grid points on the CFD grid, implying that the Riemann-style flux calculator will not resolve properly any structures of this size or smaller. Indeed, the spectral analysis shows that it is actually injecting white noise into the solution at this scale, since the energy content is actually higher than the analytic solution.

This finding is a potentially concerning one for doing high quality LES/DNS, since the Riemann flux must be hybridised with the ASF scheme in order to handle shockwaves and other discontinuities. To investigate the effect of this hybridisation, the same spectral analysis has also been performed using various levels of blending between the two fluxes, which is shown in figure 3 in grey. This shows that the

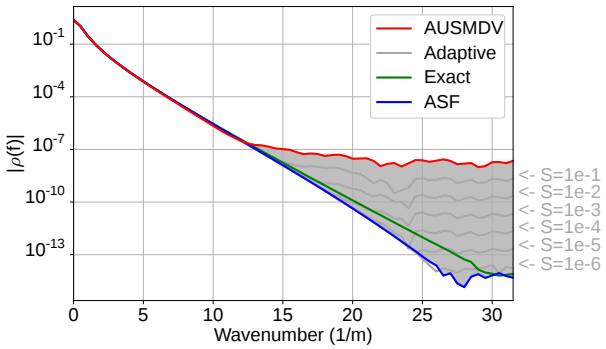

Fig 3. Fourier transform of density, absolute value against wavenumber (1/m). Taken at t=0.5

wave space solutions are more-or-less linear combinations of each other, implying that small amounts of hybridisation will not ruin the scheme's behaviour, as long as the switching parameter S can be kept small in the smooth regions of the flow.

4. Supersonic Mixing Layer Description

The flow problem studied in this work is a high-velocity time-developing reacting mixing layer taken from the work of Ref. [1], shown in figure 4. The flow domain consists of a 2cm x 2cm x 2cm cube that is periodic in the x and y directions, with opposing streams of preheated fuel and oxidiser that are initially separated by a sinusoidal perturbation.

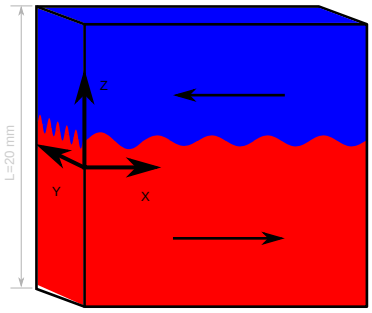

Air:

	Hydrogen:		Hydrocarbon:
p	101,000 (Pa)	p	101,000 (Pa)
T	1,400 (K)	T	1,400 (K)
u	-1,168.89 (m/s)	u	-500 (m/s)
Y_{N_2}	0.767	Y_{N_2}	0.767
Y_{O_2}	0.233	Y_{O_2}	0.233

Fuel:

	Hydrogen:		Hydrocarbon:
p	101,000 (Pa)	p	101,000 (Pa)
T	1,500 (K)	T	1,500 (K)
u	1,665.89 (m/s)	u	634.3 (m/s)
Y_{H_2}	1.0	$Y_{C_2H_4}$	1.0

Fig 4. Supersonic Mixing Layer Initial Conditions. (Interface perturbations are exaggerated.)

At time zero the two fluid streams begin to interact, and a cascade of fluid instabilities begins that eventually forms a layer of reacting turbulent flow, that first mixes and then burns the two streams to produce a complex but tractable simulacrum of the mixing and combustion occurring in a scramjet engine. The original flow conditions are maintained for the hydrogen-fuelled case, but for the hydrocarbon one the stream velocities have been reduced to keep the same convective Mach number M_c. M_c is a dimensionless parameter that approximately predicts the growth rate of compressible mixing layers, as dicussed by Ref. [11].

Simulations are run for 100 microseconds, the point at which the mixing layer becomes large enough to start being noticeably adulterated by the domain's periodic boundaries. Time advancement is performed using the three-stage explicit Runge-Kutta scheme and a CFL number of 0.5, with operator splitting approach for the chemistry, a method in which an adaptive explicit substepping method advances the reactions in time using many small steps for each fluid step. These reactions are modelled using the 13 species, 33 reaction hydrogen oxidation model of Jachimowski [12] for the hydrogen case, and using the 6 species, 3 reaction model of Baurle and Eklund [13] in the hydrocarbon case. Differential diffusion is modelled using species specific Lewis numbers that are taken from the GDTk gas library [2].

5. Supersonic Mixing Layer Results

The primary story developed in this section is that the two mixing layer solutions show a number of striking differences that are consistent with the characteristics of their fuels. Hydrogen is a light gas and reacts comparatively quickly, leading to an unusual asymmetric layered structure with most of the intense combustion happening on the lean side. In contrast the ethylene flow develops more slowly and stably, into a layer of nonpremixed combustion that is constrained by the mixing rate. In both cases the initial development of the mixing layer is chaotic and difficult to characterise, though this issue settles down as the flow develops.

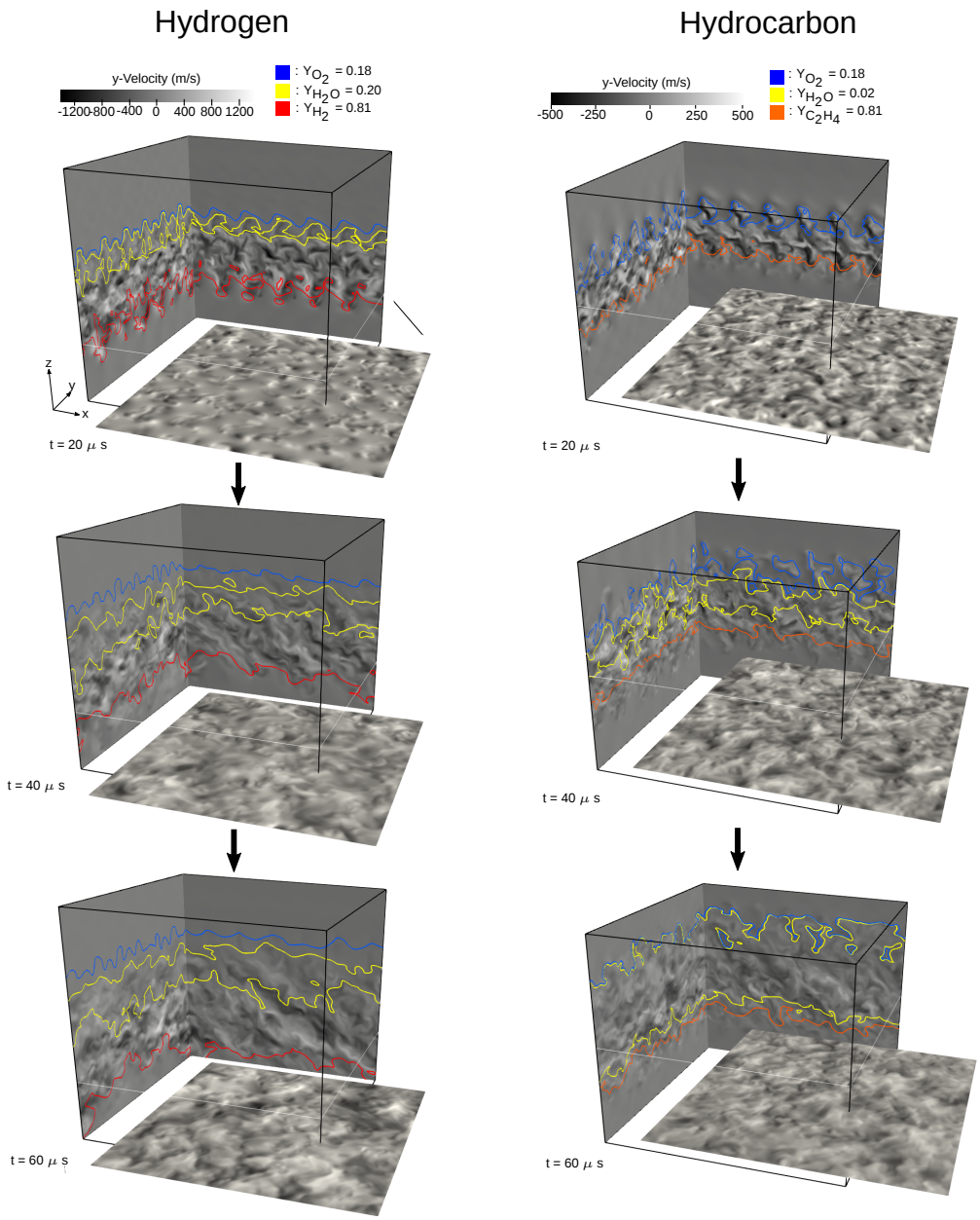

Fig 5. Isometric surface plots of y-velocity, with contours of chemical species. Left: Hydrogen case. Right: Hydrocarbon case.

Figure 5 shows a cutaway view of the domain at three separate times, with a greyscale map of the y direction velocity, and contours of different species indicated in colour. Since the mean velocity in the y direction is zero, the visualisation shows the development of the unsteady turbulent structures, which are visibly irregular by the 40 μ s time in both cases. The colours also show the lean-side dominance of H_2O in the hydrogen case, and the much slower combustion in the hydrocarbon one: note the contour level is an order of magnitude lower.

5.1. Flame Index and Heat Release Rate

Combustion flows are often categorised on a spectrum between two idealised regimes, ranging from premixed combustion in a perfectly mixed flow at one end, to nonpremixed combustion in a totally separated diffusion flame at the other. Real combustion cases are sometimes difficult to classify on this spectrum, or may have to be analysed after the fact to determine which, if any, regime they belong to. A commonly used quantity to assess this problem is the Takeno Flame Index (TFI) [14], which is computed using the dot product of the fuel and oxidiser mass fraction gradients.

$$TFI = \nabla Y_F \cdot \nabla Y_{\text{Ox}} \tag{21}$$

Positive values of TFI occur where the two gradients are in alignment, and the fuel and oxidiser travel together into the reaction front. This indicates premixed combustion. Conversely, a negative TFI indicates fuel and oxidiser diffusing toward each other in opposite directions, a characteristic of nonpremixed combustion. The magnitude of the index is also interesting, as it gives a measure of how intense the reactions are at each location. Figure 6 shows slices of the TFI computed from both cases, averaged over the y direction to partially smooth out the turbulent fluctuations.

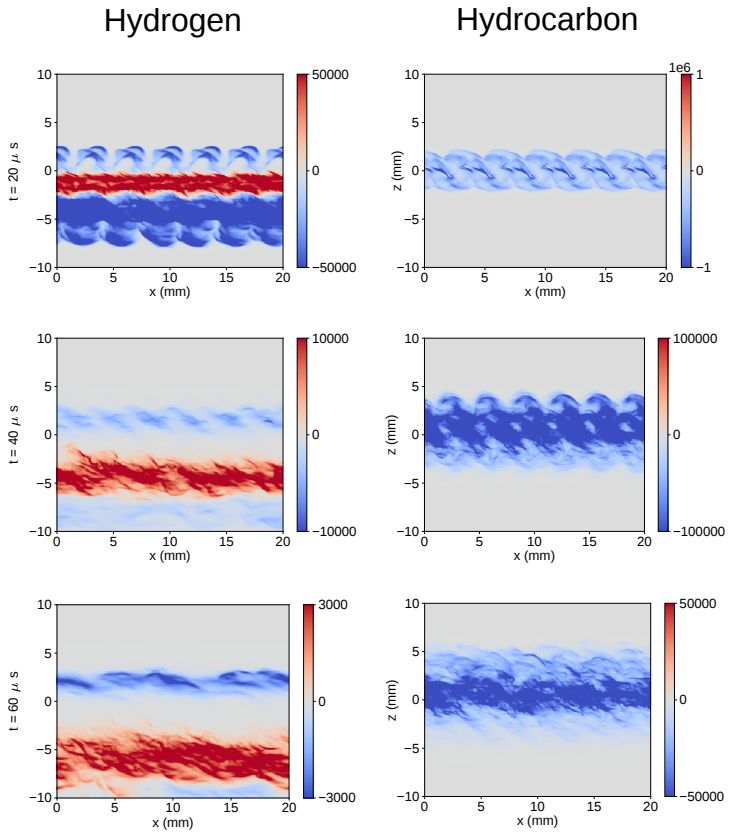

Fig 6. Takeno Flame Index (TFI) averaged in the y direction. Left: Hydrogen case. Right: Hydrocarbon case.

Merely visualising the regions of TFI can sometimes give a misleading impression of the combustion dynamics. Combustion affects the fluid dynamics of the flow mostly by releasing heat that increases the flow temperature, and this heat release may be concentrated in one mode or another. The following analysis computes the instantaneous rate of chemical heat release in each cell in the simulations, by multiplying the production rates of each species $M_s\dot{\omega}_s$ by its heat of formation h_s^f, and summing over the entire roster of chemical species.

$$\dot{H} = V \sum_s M_s \dot{\omega}_s h_s^f \tag{22}$$

Where V is the volume of a given cell. This value $\dot{H}$, the extrinsic heat release rate, is then summed using bins that depend on the flame index, to determine which kind of combustion, premixed or nonpremixed, is having the greater effect on the flow. To do this, we need a slight modification of the Flame Index referred to as the Flame Angle (TFA), which is just the angle between the fuel and oxidiser vectors, stripped of the impact of magnitude.

$$TFA = arccos\left(\frac{\nabla Y_F \cdot \nabla Y_{\mathrm{Ox}}}{|\nabla Y_F||\nabla Y_{\mathrm{Ox}}|}\right) \tag{23}$$

The polar plots in figure 7 show the sum total of the heat release occurring at each angle, for different times in the two simulations.

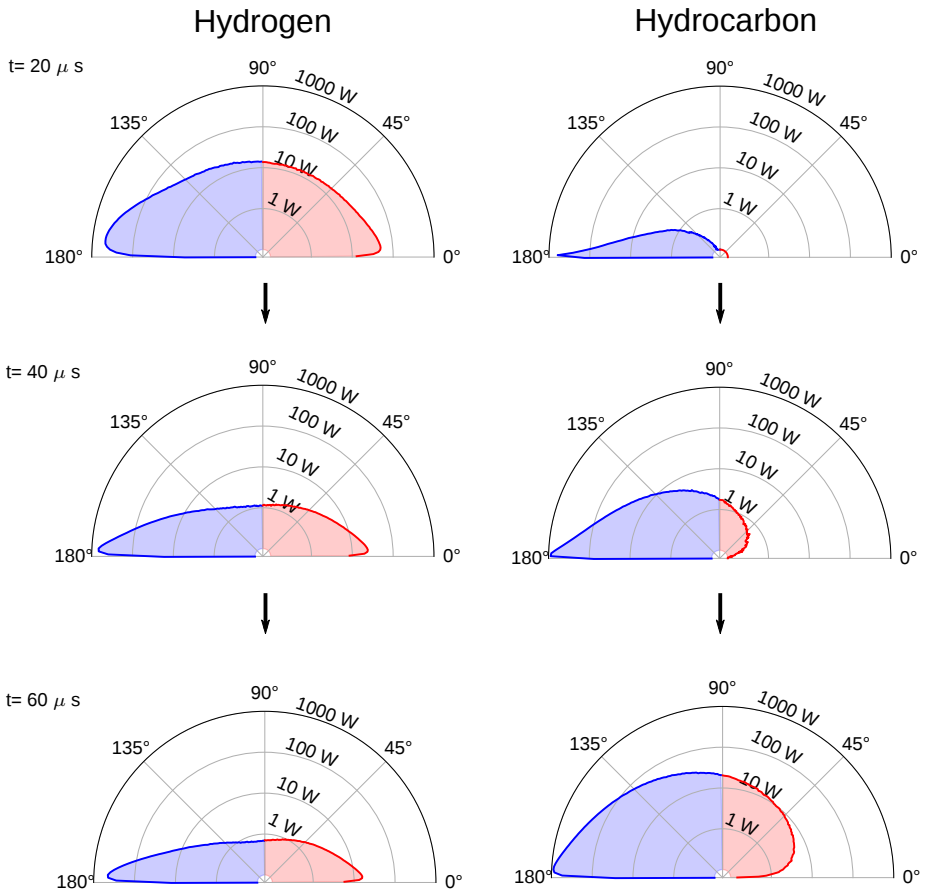

Fig 7. Summed heat release at each flame index angle. Left: Hydrogen case. Right: Hydrocarbon case.

Note that the radial coordinate of these figures uses a logarithmic scale, indicating that in both cases, the majority of the heat release occurs in the nonpremixed direction. Also of interest is that, the two cases show opposite trends in another regard: The hydrogen mixing layer has higher heat release initially and then slowly relaxes into a smaller and flatter distribution, while the hydrocarbon one slowly builds up more heat release over time, as well as forming a less clear cut distribution with more heat release occurring at intermediate angles.

5.2. Conditional Statistics

An influential class of closure models for modelling turbulent chemistry are those based on Conditional Moment Closure, or CMC [15]. These models rely on the assumption that some difficult to model quantities, such as the species mass fractions and temperatures, tend to be correlated with easier to model quantities such as the mixture fraction. This means that the temperature and species mass fractions can be expressed as fluctuations about the conditional mean of the mixture fraction, fluctuations which are smaller in magnitude than their unconditional counterparts, and can therefore be treated as small and successfully ignored when calculating the filtered chemical reaction rates.

Incidentally, the mixture fraction, Z, is a concept from premixed combustion defined as the mass fraction of gas originating from the fuel stream. In this work it is computed by summing up mass fractions of each species, weighted by the contribution of Hydrogen or Carbon atoms in each one. This definition is formalised below, and introduces the atomic composition matrix a_s^i, where for example, H_2O would have the value $a_{H2O}^H = 2$

$$Z = \sum_s Y_s \left(a_s^H \frac{M_H}{M_s} + a_s^C \frac{M_C}{M_s} \right) \tag{24}$$

This work is part of an effort to extend CMC based modelling to highly compressible flows, though there are outstanding questions about which assumptions are actually valid in high speed flow, and how best to model the subgrid distribution of the conditioning variable. In this section, conditional statistics are calculated from the compressible mixing layers, focusing on the mixture fraction as the conditioning variable, as the results so far imply nonpremixed combustion appears to be the more important regime.

For the hydrogen mixing layer OH is considered, merely as an example of an intermediate species of interest, and the hydrocarbon mixing layer we focus on H_2. In both cases, the temperature is also of interest.

The data are collected using heatmaps that count the number of occurrences of a data point in a 500x500 set of bins that span the space of interest. This essentially acts as a scatter plot, however it prevents the problem where a large enough mass of data can saturate the available pixels and produce a misleading visual representation of the dataset.

Plotted over the top of each heatmap is a separately computed curve that bins the data according mixture fraction only. The grey dots are the mean of each bin, otherwise known as the conditional mean, and the dotted lines above and below are 90 % variation intervals, computed using the standard deviation of each bin and assuming the variation is normally distributed. The curve created by joining these means is the conditional relationship between each variable and the mixture fraction, and the tightness of this relationship is the correlation between variables that CMC relies on.

In the case of the intermediate species plotted in figure 8, the later times show a fairly tight correlation in roughly the expected shape, but the early times are visibly less correlated, particularly in the hydrocarbon case, which has a bizarre distribution with extremely large variations from the mean.

To quantify these impressions, we have developed a measure of the tightness of the conditional averaging called the Total Conditional Variation. This quantity is defined as the area between the two dotted curves (computed using the trapezoid rule), divided by the total area of their bounding box. In a perfectly correlated flow this quantity would approach zero, while in a completely uncorrelated one it approaches one.

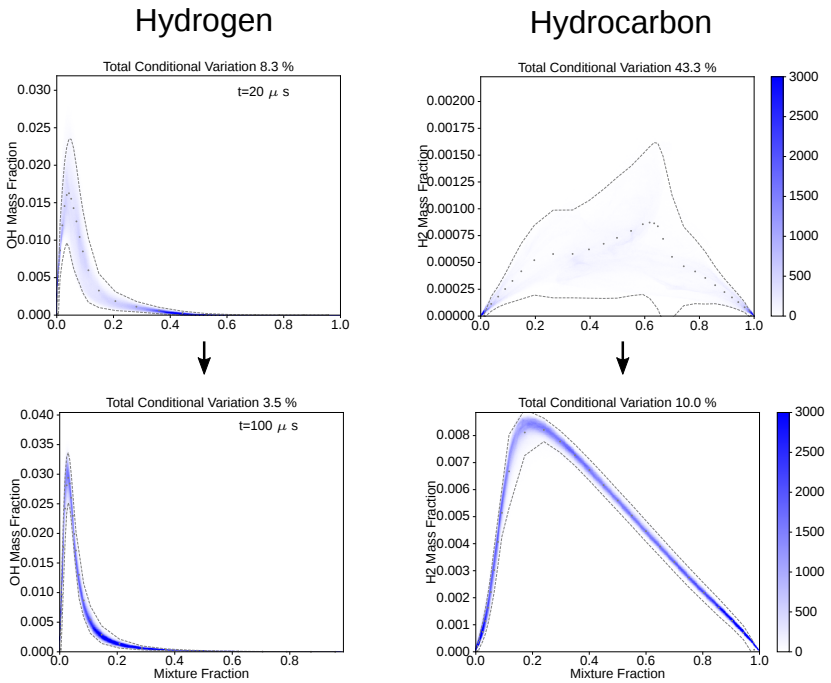

Fig 8. Intermediate species vs. Mixture Fraction heatmaps. Left: Hydrogen case. Right: Hydrocarbon case.

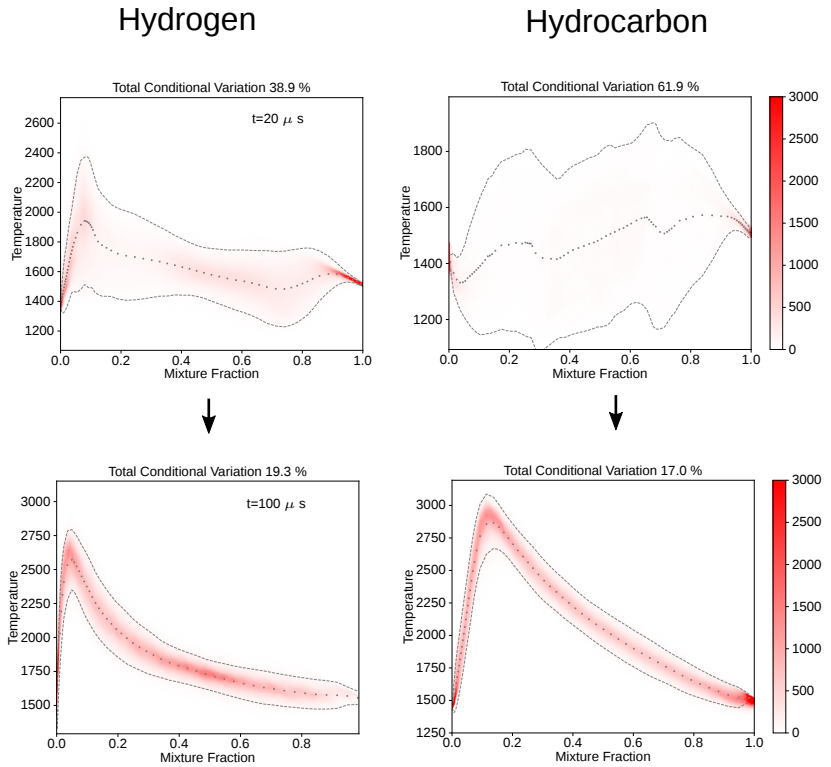

Fig 9. Radical species vs. Mixture Fraction heatmaps. Left: Hydrogen case. Right: Hydrocarbon case.

Comparison of the Total Conditional Variation reveals that the temperatures are much less correlated with mixture fraction that the species mass fractions, even at later times once the combustion has settled down. Conditional variation on the order of hundreds of degrees is present in both cases, which may prove to be a significant error in first order CMC, at least if no mitigating adjustments can be made.

6. Conclusions

This work has developed a compressible turbulent mixing layer problem that is intended to be a test bed for investigating the physics of high velocity turbulence/chemistry interaction. Simulations of this problem can use a small domain and periodic boundary conditions to create a tractable flow problem that can be studied with Direct Numerical Simulation, and in doing so create datasets that can be used for developing new models for the turbulence/chemistry closure problem.

A key challenge in compressible DNS is developing a numerical method than can handle shockwaves and other discontinuities, while also having low dissipation in smooth regions of the flow. To this end we have developed a novel hybridisation scheme that splits the task of detecting discontinuities between two functions: one detector for shockwaves and another for contact surfaces. This approach proved successful in the large scale DNS calculations, though extra analysis using the Steepening Wave problem has confirmed that the hybridisation does potentially adulterate the performance of the low-dissipation scheme. These results show that careful tuning and adjustments to one's discontinuity criteria should be performed to maximise the quality of the subsequent compressible DNS/LES simulations.

The actual simulated mixing layers reveal a number of striking differences between the hydrogen case and the hydrocarbon fuelled one, including in their reactant/product structure as well as premixedness vs. nonpremixedness. Although some effort was made to keep the fluid dynamics of the two cases the same, the Convective Mach Number of the two conditions is quite high, on the order of 0.76. Ref. [11] note that compressible mixing layer growth rates collapse below an M_c value of 0.6, but above this number three-dimensional, and non-linear, wave modes are present that cause different behaviour. This means that it is difficult to isolate the effect of chemistry from the fluid dynamics in the present work, though in both cases there are still some interesting statistical results that can inform future model development. In particular, both cases show large variation of the temperature with respect to conditional mixture fraction, which will have implications for developing a version of Conditional Moment Closure that works well for highly compressible flows. Such a method may have to identify an additional conditioning variable that can account for this variation, or else find some other method of modelling the conditional variation of T directly.

References

[1] N. N. Gibbons, *Simulation and Dynamics of Hypersonic Combustion*. PhD thesis, The University of Queensland, School of Mechanical and Mining Engineering, St Lucia, QLD 4072, 2019.

[2] N. N. Gibbons, K. A. Damm, P. A. Jacobs, and R. J. Gollan, "Eilmer: An open-source multi-physics hypersonic flow solver," *Computer Physics Communications*, vol. 282, no. 108551, 2023.

[3] L. Whyborn, *Direct numerical simulations of instabilities in the entropy layer of a hypersonic blunted slender cone*. PhD thesis, The University of Queensland, School of Mechanical and Mining Engineering, St Lucia, QLD 4072, 2023.

[4] R. J. Gollan, *The Computational Modelling of High-Temperature Gas Effects with Application to Hypersonic Flows*. PhD thesis, The University of Queensland, School of Mechanical and Mining Engineering, St Lucia, QLD 4072, 2008.

[5] T. C. Fisher, M. H. Carpenter, J. Nordström, N. K. Yamaleev, and C. Swanson, "Discrete conservative finite-difference formulations for nonlinear conservation laws in split form: Theory and boundary conditions," *Journal of Computational Physics*, vol. 234, September 2012.

[6] J. A. White, R. A. Baurle, T. C. Fisher, J. R. Quinlan, and W. S. Black, "Low-dissipation advection schemes designed for large eddy simulations of hypersonic propulsion systems," in *48th AIAA/ASME/SAE/ASEE Joint Propulsion Conference and Exhibit*, September 2012.

[7] A. Honein and P. Moin, "Higher entropy conservation and numerical stability of compressible turbulence simulations," *Journal of Computational Physics*, vol. 201, December 2004.

[8] Y. Wada and M.-S. Liou, "A flux splitting scheme with high-resolution and robustness for discontinuities," in *32nd AIAA Aerospace Sciences Meeting and Exhibit*, no. AIAA-94-0083, (Reno, Nevada), January 1994.

[9] E. Toro, M. Spruce, and W. Speares, "Restoration of the contact surface in the hll-riemann solver," *Shock Waves*, vol. 4, pp. 25–34, 1994.

[10] L. D. Landau and E. M. Lifshitz, *Fluid Mechanics*. Butterworth-Heinemann, 2nd ed., 1987.

[11] N. D. Sandham and W. C. Reynolds, "Compressible mixing layer: Linear theory and direct simulation," *AIAA Journal*, vol. 28, no. 4, pp. 618–624, 1990.

[12] C. J. Jachimowski, "An analysis of combustion studies in shock expansion tunnels," Tech. Rep. NASA TP-3224, National Aeronautics and Space Administration, Hampton, Virginia, July 1992.

[13] R. A. Baurle and D. R. Eklund, "Analysis of dual-mode hydrocarbon scramjet operation at mach 4-6.5," *Journal of Propulsion and Power*, vol. 18, pp. 990–1002, September-October 2002.

[14] H. Tamashita, M. Shimada, and T. Takeno, "A numerical study on flame stability at the transition point of jet diffusion flames," *Symposium (International) on Combustion*, vol. 26, no. 1, pp. 27–34, 1996.

[15] A. Y. Klimenko and R. W. Bilger, "Conditional moment closure for turbulent combustion," *Progress in Energy and Combustion Sciences*, vol. 25, pp. 595–687, 1999.